UCLA
UCLA Previously Published Works

Title

Phosphatidylserine-Incorporated Exosome Mimetics Encapsulating CXCR3 Antagonist Alleviate Osteoporosis

Permalink

https://escholarship.org/uc/item/1mj0z65m

Authors

Kang, Minjee

Li, Zhi

Chang, Insoon

et al.

Publication Date

2024-05-19

DOI

10.1002/adfm.202402521

Copyright Information

Peer reviewed

Phosphatidylserine-Incorporated Exosome Mimetics Encapsulating CXCR3 Antagonist Alleviate Osteoporosis

Minjee Kang, Zhi Li, Insoon Chang, Changlu Xu, Michelle Chiang, Lauren Kim, Yutong Wu, Jiabing Fan, Tara Aghaloo,* and Min Lee*

Exosomes derived from mesenchymal stem cells are an active area of research due to their therapeutic potential in treating osteoporosis. To further harness their therapeutic performance in modulating bone resorption, equipped exosomes with osteoclast-targeting moieties on their surface as well as chemokine receptor antagonists blocking osteoclast recruitment. Phosphatidylserine (PS), a membrane lipid exerting immunosuppressive and phagocytic signals, is incorporated in the membrane of exosome mimetics (EMs) to achieve a marked affinity for osteoclast precursors and potential anti-resorptive effects. This is also aimed to tackle a CXCL9-CXCR3 ligand-receptor axis, a critical signaling axis in regulating osteoclast precursor recruitment and differentiation at bone resorption sites, by encapsulating a chemical antagonist of CXCR3, AMG487, in the PS-incorporated EMs (PS-EMs). The osteoclast-targeting PS-EMs loaded with AMG487 effectively protected against bone loss in an ovariectomized mouse model. These findings demonstrate the great promise of PS-EMs as anti-resorptive nanotherapies for alleviating osteoporosis.

1. Introduction

Osteoporosis is the most common chronic metabolic bone disease, characterized by increased bone fragility and morbidity.[1] Osteoporosis commonly occurs in postmenopausal women and older adults, resulting from an imbalance between bone formation and bone resorption. Despite its devastating socioeconomic impact,[2] current therapeutic options for osteoporosis have limitations, often leading to various side effects.[3] One of the most severe side effects caused by current therapeutic options (bisphosphonates or denosumab) is medication-related osteonecrosis of the jaw (MRONJ).[4] Recent studies reported that the pathogenesis of MRONJ can be attributed to the imbalanced polarization of macrophages as a result of bisphosphonate-mediated immunity dysfunction.[5]

Consequently, there is an urgent need for safer treatment alternatives for osteoporosis to mitigate the potential risks associated with current therapy. Exosomes derived from mesenchymal stem cells (MSCs) have emerged as a promising therapeutic option for osteoporosis and skeletal disorders.[6] Exosomes, extracellular vesicles of 30–150 nm in size, are released following the fusion of multivesicular bodies (MVBs) with the plasma membrane.[7] They are considered to be minimally immunogenic due to their endogenous origin from parent cells.[8] Indeed, the repeated administration of MSC-derived exosomes in a patient with

M. Kang, Z. Li, C. Xu, M. Chiang, L. Kim, M. Lee
Division of Oral and Systemic Health Sciences
School of Dentistry
University of California
Los Angeles, CA 90095, USA
E-mail: leemin@ucla.edu

I. Chang
Division of Regenerative and Reconstructive Sciences
School of Dentistry
University of California
Los Angeles, CA 90095, USA

Y. Wu
Department of Chemistry and Biochemistry
University of California
Los Angeles, CA 90095, USA

J. Fan
Department of Pharmaceutical Sciences
School of Pharmacy and Health Professions
University of Maryland Eastern Shore
Princess Anne, Maryland 21853, USA

T. Aghaloo
Division of Diagnostic and Surgical Sciences
School of Dentistry
University of California
Los Angeles, CA 90095, USA
E-mail: taghaloo@dentistry.ucla.edu

M. Lee
Department of Bioengineering
University of California, Los Angeles
Los Angeles, CA 90095, USA

**ADVANCED
SCIENCE NEWS**

www.advancedsciencenews.com

**ADVANCED
FUNCTIONAL
MATERIALS**

www.afm-journal.de

graft-versus-host disease (GvHD) was well-tolerated, devoid of side effects, and resulted in patient response.[9] Exosomes derived from MSCs have demonstrated the ability to ameliorate osteoporosis by promoting angiogenesis and osteogenesis through the transfer of bioactive molecules, including proteins, lipids, and nucleic acids.[10–13]

While exosomes inherently possess therapeutic potential by themselves, efforts to engineer them have been actively explored in biomedical applications.[14–16] Two primary approaches involve either leveraging their endogenous communication system by loading exogenous cargo or by endowing additional functionality through surface engineering. Currently, several clinical trials of exosomes as therapeutic carriers are underway.[17] Surface engineering is aimed at introducing a wide array of molecules onto exosomal surfaces, including targeting moieties and polyethylene glycol (PEG) for extended circulation. However, this endeavor remains challenging due to the complexity of exosomal membrane surfaces. One promising strategy involves fusing exosomes with lipid membranes or liposomes, offering a simple yet highly versatile approach with a functionalized hybridized surface and improved cargo loading efficiency.[18–20] For instance, Lin et al. utilized incubating exosomes with plasmid-carrying exosomes as a suitable method to encapsulate the large plasmid (CRISPR/Cas9) into exosomes.[20]

In this work, to further harness their therapeutic performance in osteoporotic conditions, we have equipped exosomes with phosphatidylserine (PS) lipids on their surface and tested their performance in an ovariectomized mouse model. PS is a naturally occurring anionic phospholipid located within the inner membrane of healthy cells. During apoptosis, PS translocates from the inner membrane leaflet to the outer leaflet, serving as an "eat-me" signal on the surface of apoptotic cells.[21] This signal is readily recognized by macrophages, facilitating effective phagocytosis. Apoptotic cells are potently immunosuppressive to avoid undesirable inflammatory responses, and consequently, externalized PS on the cell is considered a global immunosuppressive signal.[22] Intriguingly, viruses and tumor cells have evolved to exploit this immunosuppressive pathway, known as PS apoptotic mimicry, as a strategy to evade host immune responses and escape immune detection.[22] We also noted the previous finding that PS receptors such as TIM4, BAI1, and STAB2 are highly expressed on the surface of monocytes/macrophages, osteoclast precursors, and bone-resorbing osteoclasts over the course of osteoclastogenesis.[23] During preosteoclast fusion, both PS externalization and PS receptors play pivotal roles in regulating the fusion process and apoptosis.[24] Thus, our approach entailed the incorporation of PS lipids into the membrane of exosome mimetics (EMs), effectively mimicking apoptotic cells and, therefore, enhancing their affinity for the osteoclast cell lineage.

Additionally, we hypothesized that these PS-presenting EMs exert anti-resorptive effects in osteoporotic conditions. Increasing evidence supports the positive effects of PS lipids on bone regeneration.[25–28] For example, Toita et al. demonstrated that PS lipids exhibit anti-inflammatory effects in macrophages, mediating M1 (inflammatory)-to-M2(anti-inflammatory) polarization of macrophages, thereby enhancing bone regeneration and osseointegration of titanium implants in rat femurs.[25] Wu et al. prepared the liposomes containing PS (PSLs) and investigated the effect of PSLs on osteoclasts, revealing that PSLs induce

an increase of TGF-β1 and PGE$_2$, leading to the inhibition of osteoclastogenesis.[26] Taken together, we have engineered EMs by incorporating PS lipids through physical fusion, anticipating their marked affinity for the osteoclast cell lineage and potential anti-resorptive effects.

We also harnessed exosomes as drug delivery carriers to potentiate their anti-resorptive effects. The chemokine ligand CXCL9 secreted by osteoblasts and receptor CXCR3 expressed on osteoclast precursors have recently been identified as an essential axis for regulating osteoclast precursor recruitment and differentiation at bone resorption sites in osteoporotic conditions.[29] The chemical antagonist of CXCR3, AMG487, has been suggested as a potential small molecule drug to suppress the migration and activation of osteoclast precursors to bone matrix.[29–32] While AMG487 has been tested in preclinical and clinical trials in psoriasis,[33] its application in addressing osteoporosis has remained unexplored. Therefore, we encapsulated AMG487 in the PS-incorporated EMs (PS-EMs) with the aim of obstructing osteoclast recruitment and ameliorating osteoporosis.

In this study, the effects of PS-EMs loaded with AMG487 drugs were pronounced in an ovariectomy-induced osteoporosis mouse model. PS-EM-AMG487s significantly contributed to the enhanced and selective uptake by macrophages, inhibition of osteoclast differentiation, and impeded migration of macrophages in vitro. PS-EM-AMG487 treatment was more effective in alleviating osteoporosis than native EMs in vivo, underscoring the promise of engineered EMs as cell-free anti-resorptive nanocarriers for osteoporosis treatment. Our study serves as a proof-of-concept for engineering exosomes via a membrane fusion approach to advance them as a novel therapeutic alternative for osteoporosis and bone immunomodulatory diseases.

2. Results and Discussion

2.1. Production and Physicochemical Characterization of PS-EMs

Phosphatidylserine-incorporated exosome-mimetics (PS-EMs) were prepared using a combination of the thin film hydration and extrusion methods, as illustrated in **Figure 1A**. To generate exosome-mimetic vesicles, mouse bone marrow-derived MSCs were extruded through a series of polycarbonate membranes with progressively reduced pore sizes. Our group previously reported that EMs generated through this extrusion approach resulted in a high yield of vesicles, exhibiting similar structural characteristics and biological internalization to conventional exosomes obtained from the culture medium.[34] Increasing evidence from other groups also suggests that membrane extrusion is an effective method to generate cell-derived exosome-mimetic nanovesicles with similar characteristics to exosomes but obtainable in large quantities.[35–37] For the relative quantitation of exosomes, the protein concentration of EMs was examined by BCA protein assay. Nanoparticle tracking analysis (NTA) was employed to obtain their corresponding number of particles (Figure S1, Supporting Information). To incorporate PS into EMs, 1,2-dioleoyl-sn-glycero-3-phospho-L-serine (DOPS) lipids dried into a thin film were hydrated in an EM-containing PBS solution. We subjected the mixture to an extrusion process to obtain a uniform and consistent size distribution of the PS-incorporated EMs, as illustrated in Figure 1A.
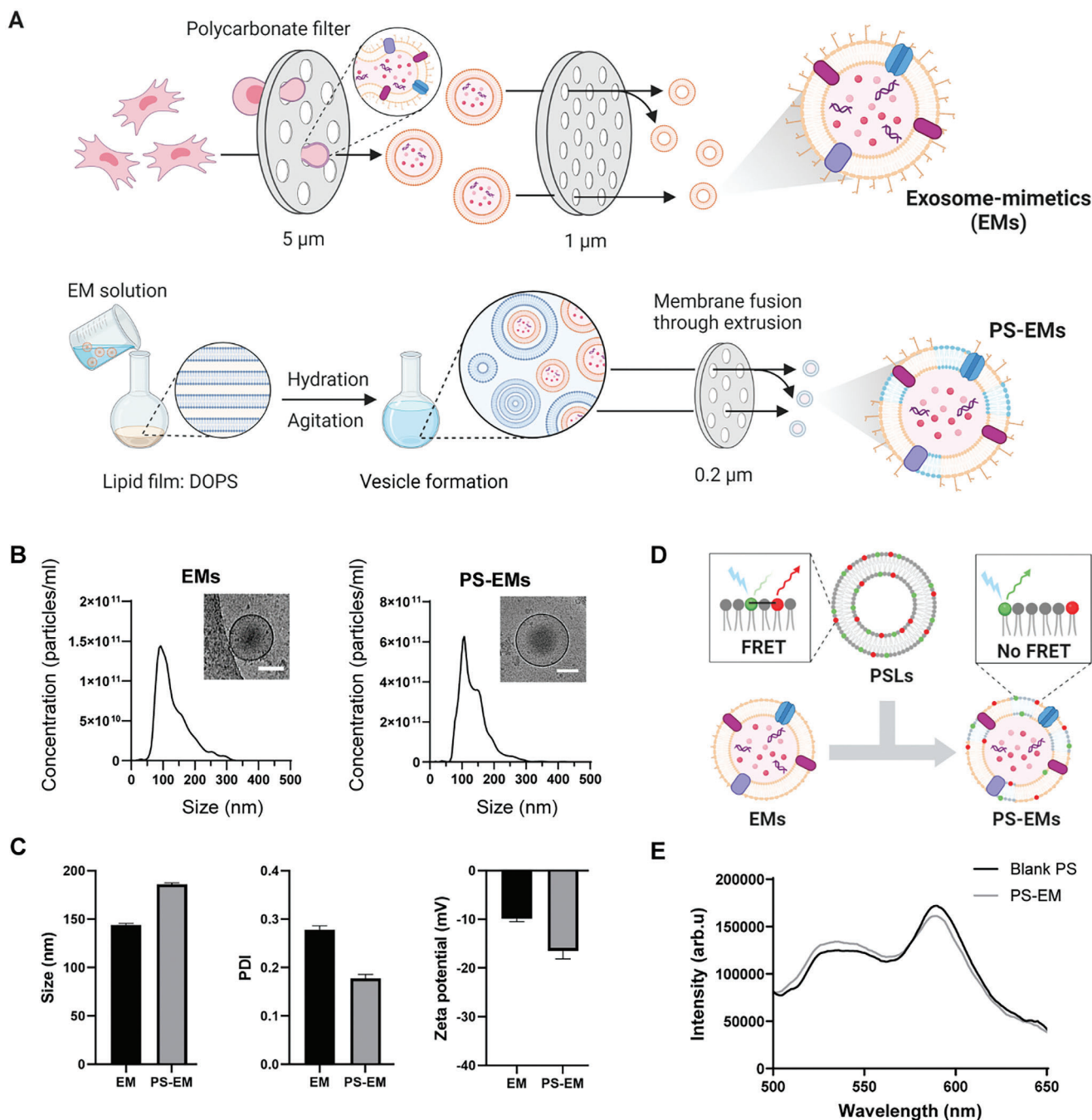
Figure 1. Preparation and characterization of PS-EMs. A) Schematic illustration of the procedure for generating exosome mimetics (EMs) and phospholipid-incorporated EMs (PS-EMs). B) Size distribution of EMs and PS-EMs revealed by Nanoparticle Tracking Analysis (NTA) with representative cryo-TEM images on top. TEM images indicate the spherical morphology (scale bar = 100 nm). C) Size, polydispersity index, and zeta potential of EMs and PS-EMs (*n* = 3). D) Schematic illustration of Förster resonance energy transfer (FRET). PSLs were doped with a FRET pair of fluorescent probes. PS-EMs, created through the fusion of EMs and PS lipids, led to FRET probe dilution. E) PSLs exhibited FRET at the acceptor emission peak (583 nm), while PS-EMs displayed fluorescence emission recovery from the donor at the lower emission peak (535 nm).

We characterized the physicochemical properties of PS-EMs and compared them with pristine EMs. Representative cryogenic transmission electron microscopy (cryo-TEM) images of both EMs and PS-EMs revealed an intact, round shape with electron-dense cargo (Figure 1B). The presence of dark spots is a characteristic feature in cryo-TEM images of exosomes containing electron-dense material. Cryo-TEM images confirmed that the vesicle structure (spherical morphology and dense inner content) was not impaired during the production process. NTA of the EMs and PS-EMs exhibited a size distribution with a mean

**ADVANCED
SCIENCE NEWS**

www.advancedsciencenews.com

**ADVANCED
FUNCTIONAL
MATERIALS**

www.afm-journal.de

diameter of 135.2 and 144.1 nm, respectively, in accordance with the outcomes of TEM analysis (Figure 1B). The average size, polydispersity index (PDI), and zeta potential of PS-EMs were further characterized using dynamic light scattering (DLS), as shown in Figure 1C. The z-average size of EMs was 144.0 nm and that of PS-EMs was 186.1 nm. The z-average size measured by DLS turned out to be larger than the NTA results, which could be attributed to the differences in the measurement techniques, as NTA shows a number-weighted distribution while DLS exhibits scattered light intensity-weighted distribution.[38] The average PDI of EM was 0.28 and that of PS-EM was 0.18. A PDI in the range of 0.1 and 0.3 is considered a narrow size distribution for pharmaceutical nanoparticle applications.[39] The average zeta potential of EMs was −9.9 mV, while that of PS-EMs was −16.5 mV. The decrease in the zeta potential of PS-EMs, given the anionic nature of PS lipids, indirectly indicates the fusion of PS lipids into the EM membrane. To confirm the incorporation of PS lipids into the membrane of EMs at the molecular level, we conducted a Förster resonance energy transfer (FRET) study. FRET occurs when two fluorophores are in close proximity (<6 nm), wherein energy is transferred from one fluorophore (donor) to another (acceptor).[40] We prepared PSLs containing a pair of fluorophore-lipid conjugates for the purpose of FRET. Upon fusion with EMs, the intermolecular distance of the FRET pair increases in the membrane, leading to a decrease in acceptor emission and an increase in donor emission, as depicted in Figure 1D. As anticipated, the emission spectrum of PS-EMs demonstrated a pronounced change when compared to PSLs (Figure 1E). PSLs exhibited FRET at the acceptor emission peak (583 nm), while PS-EMs displayed fluorescence emission recovery from the donor at the lower emission peak (535 nm), indicating the successful incorporation of PS lipids into the membrane of EMs. The incorporation efficiency of PS lipids into EMs was determined using PS lipid films labeled with a fluorophore and measuring fluorescence in the supernatant of the final extruded samples. A high incorporation efficiency of over 90% was achieved at various PS-to-EM mass ratios (Figure S2, Supporting Information).

2.2. Preferential Uptake of PS-EMs by Macrophages

We employed confocal laser scanning microscopy (CLSM) to observe the cellular uptake behavior of PS-EMs in a co-culture of hMSCs and RAW264.7 cells. Notably, PS-EMs exhibited predominant internalization by macrophage cells as opposed to hMSCs as shown in **Figure 2A**. To ensure that this preferential uptake is attributed to the PS component rather than macrophage cell characteristics, we prepared PC-EMs as a control, wherein DOPC (1,2-Dioleoyl-sn-glycero-3-phosphocholine) lipids were incorporated into the EM membranes. DOPC lipids possess an identical lipid tail structure but differ in headgroup composition compared to DOPS lipids (choline group vs serine group), making them an excellent control. Shat et al. also reported a similar trend, demonstrating enhanced uptake efficacy of PS-coated acetylated dextran nanoparticles in macrophages when co-cultured with adenocarcinoma A549 cells.[41]

To compare internalization levels between PC-EMs and PS-EMs more comprehensively, we performed semi-quantification of images using Fiji Image J (Figure 2B). The integrated fluorescence intensity, which represents the uptake of PS-EMs (or PC-EMs), was normalized to the cellular area and manually delineated on the overlay brightfield image. This semi-quantification allowed us to calculate and compare the uptake levels of EMs in both hMSCs and RAW264.7 cells. After 2 h of incubation, the internalization ratio of macrophages to hMSCs for PC-EMs was ≈2.7. In contrast, PS-EMs exhibited a significantly higher internalization ratio of 17.3, highlighting their preferential uptake by macrophages (Figure 2C). After an incubation period of 24 h, although the pattern of cellular uptake became more varied, PS-EMs continued to be selectively internalized by macrophages (Figure 2D). This difference underscores the novelty of PS-EMs wherein their distinctive feature lies in the inherent capacity of PS to enhance the cellular uptake by macrophages. CLSM imaging experiments demonstrated the predominant internalization of PS-EMs by macrophages, as compared to control PC-EMs.

We also evaluated the uptake kinetics of PS-EMs in different cell lines under similar culture conditions (Figure S3, Supporting Information). After 1 h of incubation, no significant difference was observed in the degree of PS-EM uptake compared to PC-EM in hMSCs and endothelial cells (HUVEC). However, RAW264.7 cells exhibited a higher degree of PS-EM internalization than PC-EMs. The uptake of PS-EM in RAW264.7 cells was noticeably higher compared to PC-EM after 4 h of incubation while this difference was not significant in other cells, demonstrating additional evidence of the specificity of PS-EMs toward macrophages.

2.3. PS-EMs Inhibit Osteoclastogenesis In Vitro

Next, we investigated the inhibitory effect of PS-EMs on osteoclast differentiation using Tartrate-resistant acid phosphatase (TRAP) staining. RAW264.7 cells were cultured with or without different formulations of PS-EMs for five days in the presence of a receptor activator for NF-kB ligand (RANKL). The number of TRAP-positive multi-nucleic cells (MNCs) peaked on day 5 in the presence of RANKL. On day 5, TRAP-positive cells with >3 nuclei were considered osteoclast-like MNCs in RAW264.7 cell cultures. As shown in **Figure 3A**, we observed that PS-EMs significantly decreased the number of TRAP-positive MNCs in a dose-dependent manner.

We prepared three different groups of PS-EMs with varying PS-to-EM ratios (5:1, 10:1, 20:1) and assessed their toxicity in RAW264.7 cells using the Alamar Blue assay (see Figure 3B). EMs did not induce toxicity; instead, they promoted proliferation in RAW264.7 cells, consistent with previous studies.[42] An increase in PS content within the PS-EM vesicles decreased macrophage cell viability, suggesting a limit on the amount of PS that can be incorporated into PS-EMs.

The inhibitory effect of PS-EMs on osteoclast differentiation was compared to pristine EMs (Figure 3C). Since MNCs vary in size, we opted for a more precise analysis by measuring the cellular area of MNCs using Fiji Image J, as opposed to counting the number of MNCs. The correlation between the number of MNCs and their cellular area of MNCs is depicted in histogram format in Figure S4 (Supporting Information). The sum of TRAP-positive MNC area was significantly reduced in the groups treated with PS-EMs (PS-to-EM ratios of 5:1, 10:1, and 20:1)
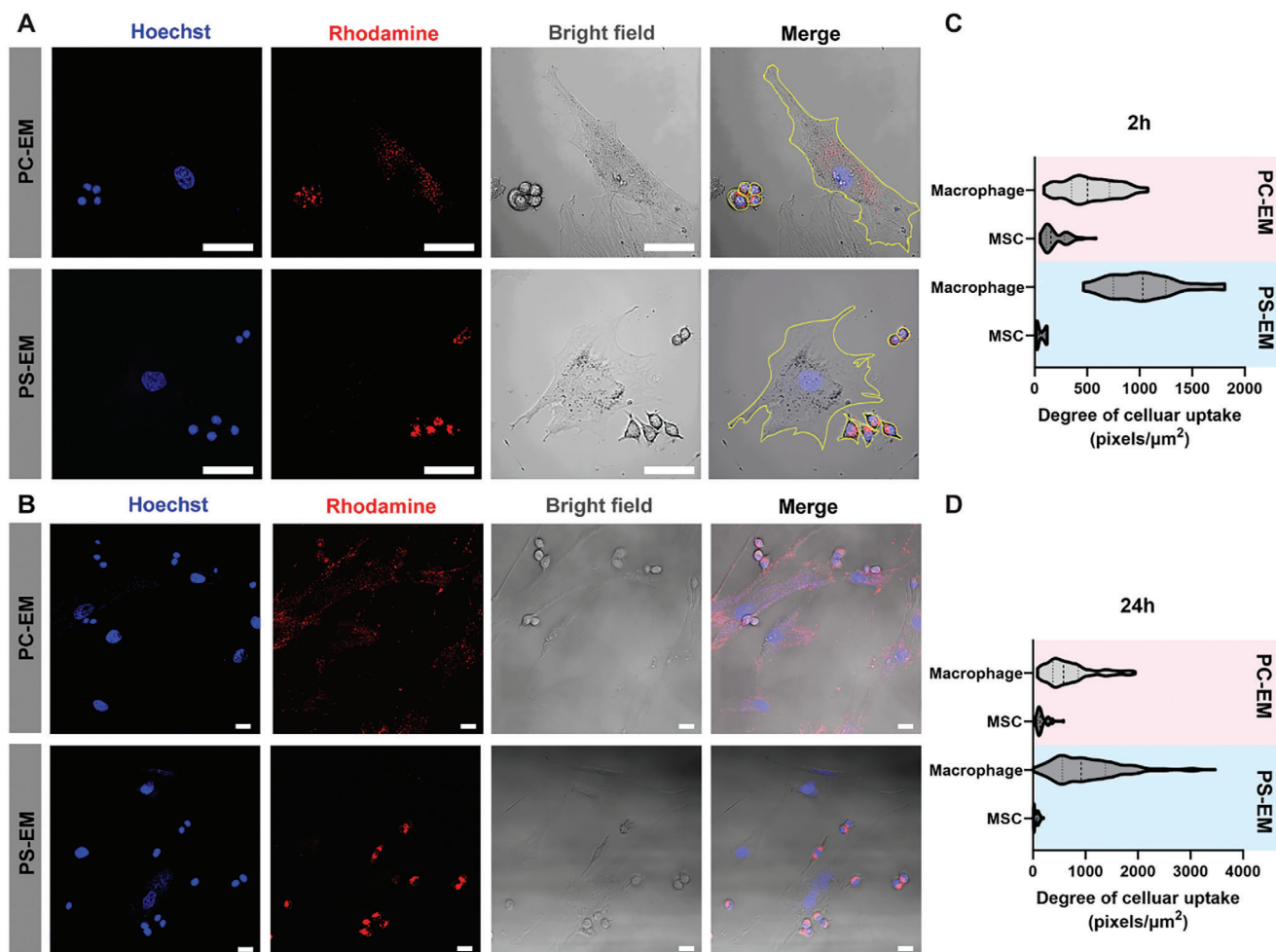
**ADVANCED
SCIENCE NEWS**

www.advancedsciencenews.com

**ADVANCED
FUNCTIONAL
MATERIALS**

www.afm-journal.de

Figure 2. Preferential uptake of PS-EMs by macrophages over MSCs in vitro. A,B) Confocal fluorescence and bright-field images of co-cultured hMSCs and RAW264.7 cells following (A) 2 h and (B) 24 h incubation with either PS-EMs or control PC-EMs. Scale bars = 20 μm in (A) and 50 μm in (B). C,D) Degree of cellular uptake analyzed using Image J software for (C) 2 h and (D) 24 h incubation periods. The sum of the pixel values in the selected area (integrated fluorescence intensity) was normalized to the cellular area to quantify the degree of PS-EM or control PC-EM uptake between MSCs and macrophages. All experiments were conducted in triplicate.

– approximately one-third in comparison to the positive control and half in comparison to pristine EMs. In groups of PS-EMs, the increased mass ratio of PS to EM resulted in enhanced osteoclastogenesis inhibition effects.
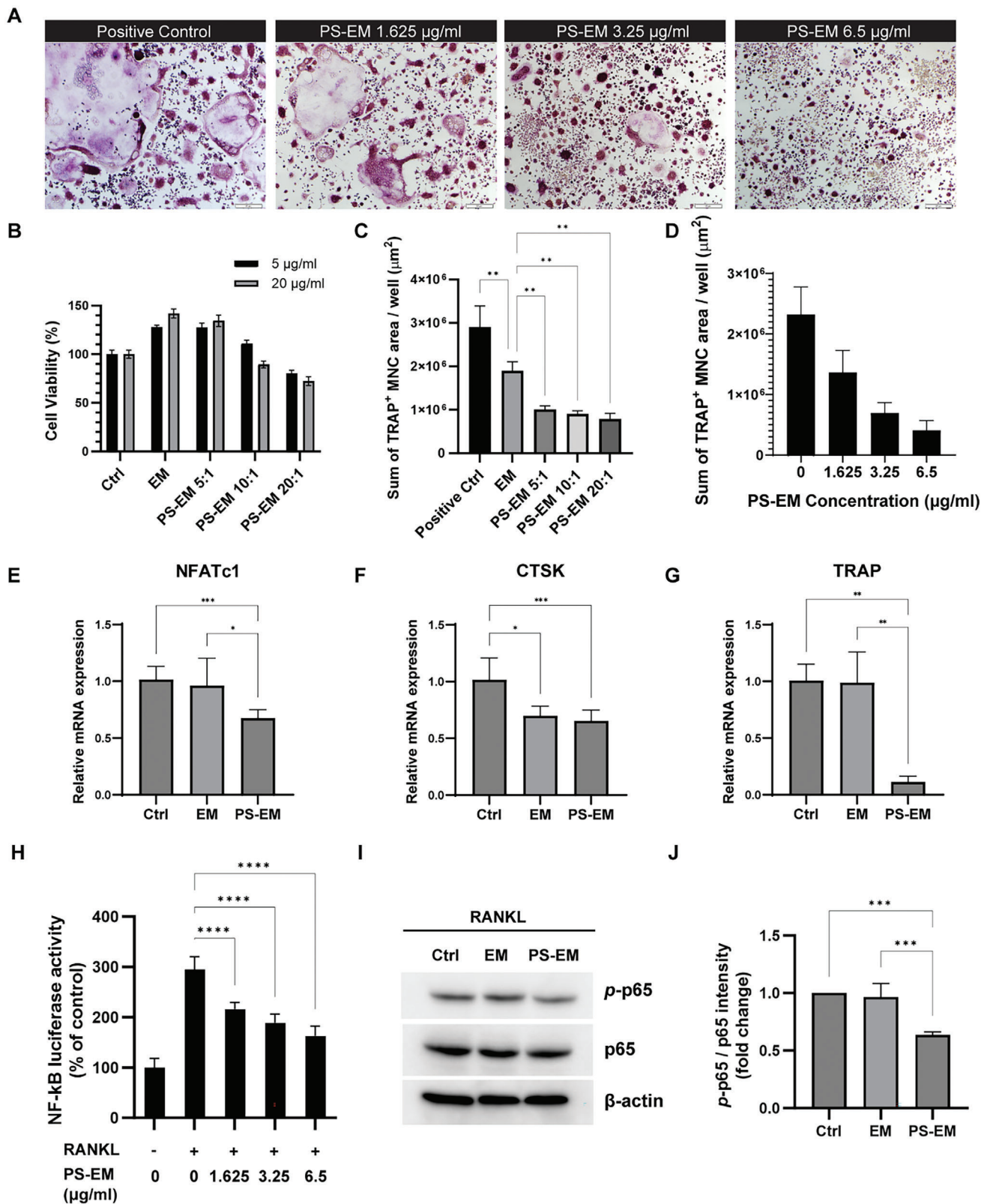
The ratio of the PS lipid (based on weights) to exosome-mimetics (based on protein contents) was optimized to 10:1 for the following experiments. The rationale behind using a PS-to-EM ratio of 10:1 was based on the finding that higher PS incorporation led to more effective osteoclast inhibition. However, PS incorporated into EMs was limited due to cytotoxicity concerns associated with high PS concentrations. Our cellular internalization studies revealed that PS-EMs have a higher affinity for binding to plasma membranes compared to control phosphatidylcholine-EMs (PC-EMs) (data not shown). Notably, excessive PS levels can lead to apoptosis due to the rapid uptake by cells, which disrupts cellular signaling. This toxic mechanism may be linked to the constant cycling of PS across plasma membranes, compromising the integrity of the plasma membrane, and ultimately leading to cell death.[43] Therefore, optimizing PS

concentrations in EM formulations is required for eventual therapeutic applications.

Quantitative analysis in Figure 3D clearly illustrates the dose-dependent reduction in the TRAP-positive MNC area upon the application of PS-EM to the RAW264.7 cell cultures. These observations strongly suggest that the incorporation of PS into EMs is a promising strategy to boost the osteoclastogenesis inhibition effect of EMs.

To further investigate the inhibitory effect of PS-EMs on osteoclast differentiation, we performed a quantitative real-time polymerase chain reaction (qRT-PCR) analysis and assessed the expression of osteoclast-related genes. Treatment of RAW264.7 cells with PS-EMs significantly down-regulated the expression of NFATc1, a master transcriptional factor for osteoclast differentiation (Figure 3E). PS-EM treatment also inhibited the expression of osteoclast markers, including cathepsin K (Ctsk) and TRAP (Figure 3F,G).

To gain insight into PS-EMs inhibit osteoclast differentiation, we examined whether PS-EM suppresses RANKL-induced NFκB

**ADVANCED
SCIENCE NEWS**

www.advancedsciencenews.com

**ADVANCED
FUNCTIONAL
MATERIALS**

www.afm-journal.de

activation using luciferase activity assay (Figure 3H). RANKL significantly induced the transcriptional activity of NFκB in RAW264.7 cells that were transfected with NFκB-luc. In contrast, treatment with PS-EMs significantly inhibited the RANKL-induced transcriptional activity of NFκB in a dose-dependent manner from 1.625 to 6.5 µg mL^{-1}. These data suggest that PS-EMs might inhibit the RANKL-induced NFκB signaling pathway and thereby contribute to the inhibition of osteoclast differentiation. To further confirm this finding, we carried out a Western blot analysis of total and phosphorylated NFκB p65 (Figure 3I,J). We found that PS inhibited p65 phosphorylation in response to RANKL in RAW264.7 cells. This finding is consistent with previous research by Doffek et al., which showed that PS inhibits the activation of NF-κB in response to lipopolysaccharides (LPS) in human monocyte-derived dendritic cells by preventing the phosphorylation and degradation of IκBα.[44] There was some degree of inhibitory effect of pristine EMs suggesting EM-mediated transfer of proteins and miRNAs regulating osteoclast differentiation. Previous research has shown that MSC-derived extracellular vesicles can inhibit osteoclastogenesis through osteoprotegerin (OPG) and miR-21-5p.[45] These findings collectively emphasize the potential of PS-EMs in blocking osteoclast differentiation.

PS-containing liposomes have been explored in osteoclastogenesis or macrophage-mediated immunomodulation to inhibit abnormal bone loss and promote bone tissue regeneration.[26,46] Conventional liposomes composed of unsaturated lipids are prone to hydrolysis and oxidation, and freezing for long-term storage is challenging due to the fragile nature of phospholipid membranes. The low chemical and physical stability can be problematic, leading to adverse effects and efficacy reduction. Moreover, liposomes in different compositions can be toxic to cells and evoke an immune response. On the other hand, cell-derived exosomes hold promise as therapeutic drug carriers due to their high biocompatibility and low immunogenicity. Exosomes are enriched in various lipids, conferring membrane rigidity and stability, and can be preserved by freezing.[47,48] In vitro cytotoxicity evaluation of PS-EMs demonstrated lower toxicity to hMSCs compared to PS liposomes when the same number of vesicles were administered (Figure S5, Supporting Information). Moreover, exosomes are endogenous nanocarriers of various signaling molecules and play an important role in mediating intercellular communications. EMs derived from MSCs have been shown to hold intrinsic osteoinductive properties with no drug loading in our previous studies.[34,49] These favorable properties make our EM-based system a promising candidate for the development of novel therapeutics for osteoporosis and other bone diseases.

2.4. PS-EMs as AMG487 Drug Delivery Carriers to Tackle CXCR3-CXCL9 Axis

We then proceeded to explore the potential of PS-EMs as drug delivery carriers. The small molecule drug chosen was AMG487, an antagonist of the CXCR3 receptor. We integrated the drug AMG487 into PS-EMs to leverage its known efficacy in inhibiting the activation of osteoclast progenitors.[29] As illustrated in **Figure 4A**, Hydrophobic AMG487 molecules were introduced into an organic lipid solution. The evaporation of the organic solvent allowed the drugs to become integrated within the lipid thin film. The subsequent extrusion process with EMs resulted in the formation of PS-EMs encapsulating AMG487. To assess drug loading efficiency, we employed UV-Vis spectrometry. A loading of 5 mol% AMG487 resulted in an 82% encapsulation efficiency, while a 10 mol% loading of AMG487 yielded a 75% encapsulation efficiency (Figure 4B). Nanocarriers with high drug payloads are preferred for higher in vivo bioavailability and therapeutic efficacy. To assess drug loading efficiency, we employed UV–vis spectrometry. A loading of AMG487 up to 10 mol% exhibited good encapsulation efficiency of over 75% (Figure 4B). In the subsequent experiments, 10 mol% loading of AMG487 was used.

AMG487 plays a critical role in inhibiting the CXCL9-CXCR3 axis.[29,31,32] This axis, involving CXCL9 (the CXC chemokine family) and its receptor CXCR3, has been recently identified to induce chemotaxis and macrophage activation – processes that are integral to the recruitment and activation of osteoclasts in osteoporosis (Figure 4C).[29] Furthermore, recent studies exploring the effects of AMG487 on rheumatoid arthritis (RA)[30] and periodontitis[32] reflect additional insight into the pathogenic and immune regulatory mechanisms of AMG487.

To investigate the effect of PS-EMs loaded with AMG487 on the migration of macrophages, we conducted a transwell migration assay (Figure 4D,E). Initially, a chemotaxis assay was performed to assess macrophage migration in response to rm-CXCL9. The results demonstrated that macrophages had migrated across the membrane when exposed to rmCXCL9 in a dose-dependent manner (Figure S6, Supporting Information). Subsequently, macrophages treated with RANKL for three days were loaded onto the upper side of the insert, as depicted in Figure 4C. The lower chamber of each transwell contained a medium with rmCXCL9, facilitating macrophage migration through the pores to the other side of the membrane. As shown in Figure 4D,E, migration was significantly enhanced by rmCXCL9 compared to the negative control group. Macrophages treated with PS-EMs did not exhibit notable differences in migration. Notably, cells treated with PS-EM-AMG487 displayed reduced

Figure 3. Inhibitory effect of PS-EMs on osteoclast differentiation of RAW264.7 cells. A) Representative microscopy images of TRAP-stained RAW264.7 cells cultured with different PS-EM concentrations. Scale bars = 100 µm. B) Alamar Blue assay to evaluate the cell viability incubated with EMs or PS-EMs for 24 h. C) Quantification of TRAP-stained multi-nucleic cells (MNCs) treated with 5 µg of EMs or various formulations of PS-EMs, highlighting the inhibitory effect of PS-EMs over pristine EMs. D) Dose-dependent inhibition of TRAP-positive MNC formation by PS-EMs (10:1 ratio). E–G) qRT-PCR analysis of mRNA expression levels of osteoclast-related genes NFATc1, CTSK, and TRAP during RAW264.7 differentiation at day 3. GAPDH was employed as an internal reference gene. H) 10:1 PS-EMs inhibited RANKL-induced NF-κB activation in NF-κB luciferase transfected RAW264.7 cells. RAW264.7 cells were pre-treated with PS-EMs for 1 h before the incubation with RANKL (100 ng mL^{-1}) for 24 h. I) Western blot representative images of control, EM-treated, or PS-EM-treated RAW264.7 cells. EMs or PS-EMs were incubated for 30 min prior to RANKL (100 ng mL^{-1}) stimulation for 24 h. Then, whole cytoplasmic and nuclear proteins were extracted as described in the methods. J) The expression levels of p-p65, p65, and actin in the cytoplasmic and nuclear extracts were determined using western blot analysis. All the data are presented as mean ± SD, $n = 3$. **$p < 0.01$, ***$p < 0.001$, ****$p < 0.0001$, one-way ANOVA with Tukey's post hoc test.
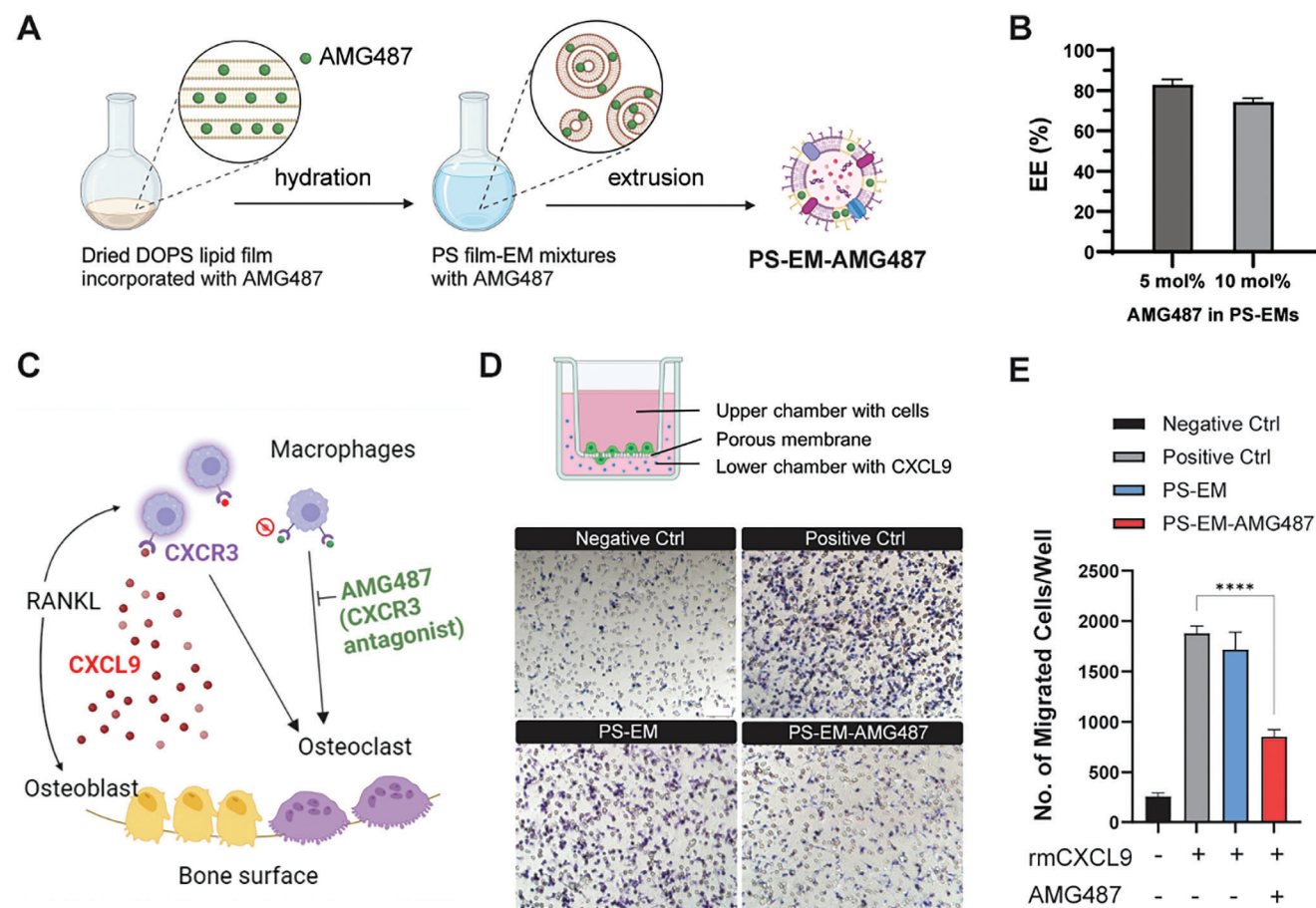
Figure 4. The inhibitory effect of CXCR3 antagonist on macrophage migration in the presence of CXCL9. A) Schematic illustrating the process of AMG487 incorporation into PS-EMs. B) The encapsulation efficiency of AMG487 in PS-EMs with 5 or 10 molar percentage of AMG487. C) Schematic depicting chemokine control of osteoclast recruitment via the CXCL9-CXCR3 axis. RANKL, either directly or indirectly, induces the release of CXCL9 from osteoblast progenitors, which activates macrophages expressing the CXCR3 receptor. This activation triggers macrophage recruitment and differentiation into osteoclasts, contributing to bone resorption. E) Representative images of mouse bone-marrow-derived macrophages that migrated through a porous membrane. Macrophages were fixed and stained using hematoxylin. Scale bar = 50 µm. F) Cell migration assay results show that bone-marrow-derived macrophages (activated osteoclast precursors) migrated through the membrane under the influence of CXCL9, except for the negative control, for 8 h. In cells pre-treated with PS-EM-AMG487, migration was significantly inhibited ($^*p < 0.0001$, unpaired student's t-test, n = 3).

migration to the membrane, indicating the inhibitory effect of AMG487 on CXCL9-induced macrophage migration. The cell migration assays indicated that PS-EMs loaded with AMG487 (PS-EM-AMG487s) successfully inhibited macrophage migration in the presence of CXCL9. These results suggest the potential of targeting the CXCR3 pathway with AMG487 to modulate the chemokine-controlled recruitment of osteoclasts.

2.5. PS-EM-AMG487 Inhibits Bone Loss in an OVX Mouse Model

In this study, we employed an osteoporotic mouse model created by ovariectomy (OVX). To investigate the therapeutic efficacy of PS-EM-AMG487s in the OVX mouse model, OVX mice were intraperitoneally injected with EMs, PS-EMs, or PS-EM-AMG487s (0.1 mg/100 µl PBS), or vehicle (PBS), once a week over the course of 8 weeks as shown in **Figure 5A**. In determining the optimal dosage of EMs, we followed precedents from previous studies. Injecting 100 µg of EMs per injection into OVX mice

was shown to effectively ameliorate bone loss in osteoporotic settings.[50–52] In determining the optimal drug loading for our PS-EMs, we considered both the maximum loading efficiency achievable and the range of drug dosages reported in similar studies. Loading efficiency is a critical factor as it directly impacts the therapeutic efficacy and safety of the drug delivery system. For PS-EMs, we aimed to maximize the amount of AMG487 loaded while ensuring the stability and functionality of the EMs. When we loaded 10 mol% of AMG487 into PS-EMs, the loading efficiency was reported to be 75% (Figure 4B), comparable to the drug loading in other liposome-based nanoparticles.[53] Future studies should continue to explore this balance, aiming to refine the drug-loading process to achieve even higher efficiency and efficacy. Such investigations could potentially expand the therapeutic applications of PS-EMs and similar nanocarrier systems in osteoporosis and other related conditions.

After 8 weeks of treatment, PET/CT scans were conducted using ^{18}F-fluoride as the radiotracer (Figure 5B). The images show accumulation of ^{18}F-fluoride in the bones including spine and

**ADVANCED
SCIENCE NEWS**

www.advancedsciencenews.com

**ADVANCED
FUNCTIONAL
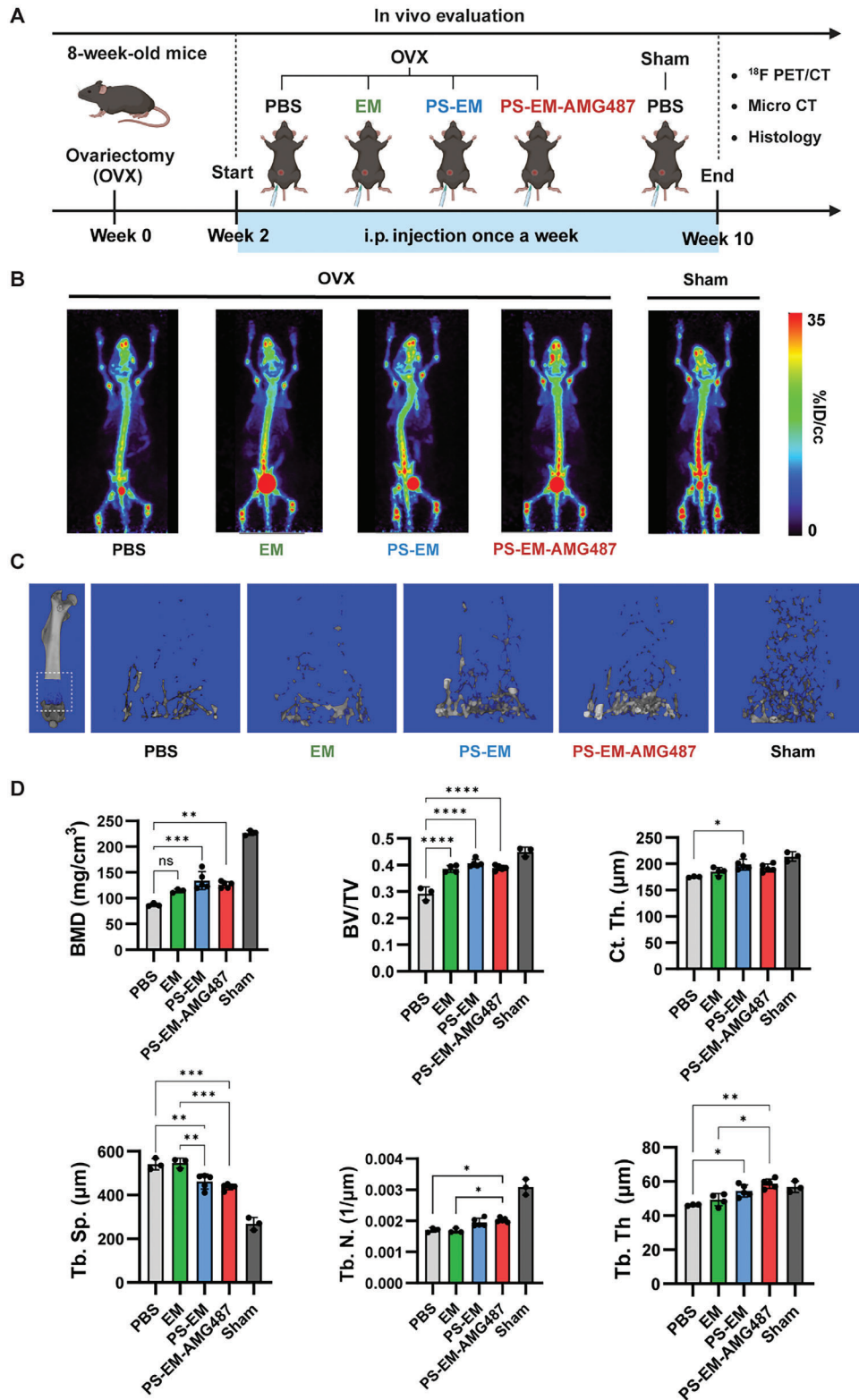MATERIALS**

www.afm-journal.de

Figure 5. PS-EM treatment ameliorated osteoporosis phenotypes in OVX mice. A) Timeline of the in vivo experiment, including the OVX model preparation, injection, and evaluation. B) Representative maximum intensity projection images of ^{18}F PET/CT data where regions of higher intensity correlate with increased bone mineral density. C) 3D μCT reconstruction images of mouse femurs. The volume of interest of trabecular bone was taken 0.5 mm proximally from the distal epiphyseal growth plate, with 3 mm in height. D) Quantitative analyses of trabecular bone microarchitecture in femora. BMD. Bone mineral density; BV/TV, percent bone volume; Tb. Sp., trabecular separation; Tb. Th., trabecular thickness, Tb. N., trabecular number. The data are presented as mean ± SD, $^*p < 0.05$, $^{**}p < 0.01$, $^{***}p < 0.005$, $^{****}p < 0.001$, one-way ANOVA with Tukey's post hoc test.

**ADVANCED
SCIENCE NEWS**

www.advancedsciencenews.com

**ADVANCED
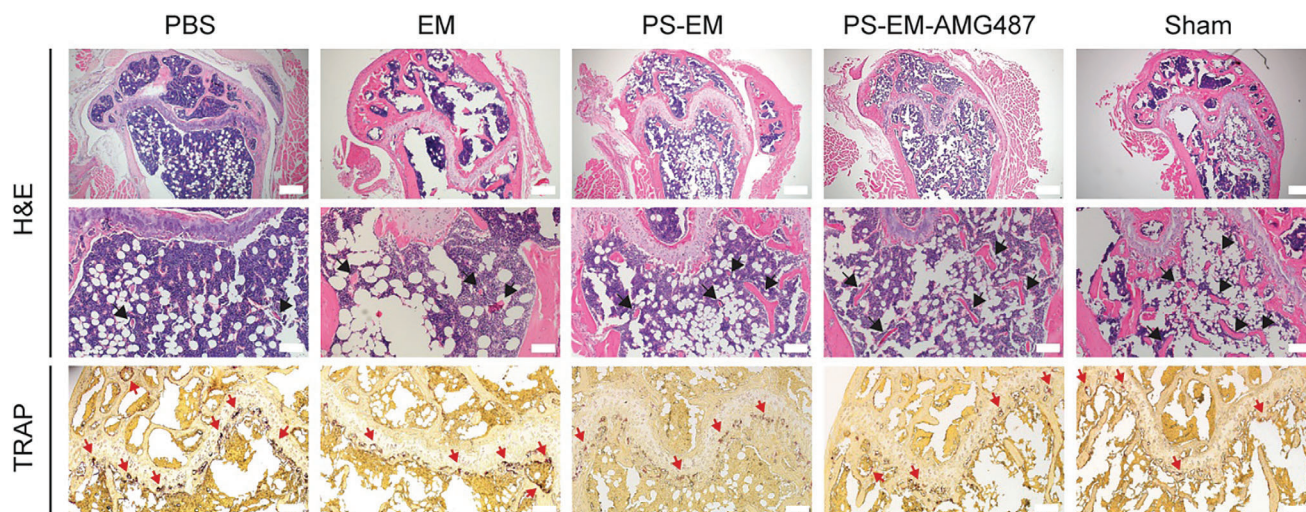FUNCTIONAL
MATERIALS**

www.afm-journal.de

Figure 6. PS-EM treatment improved the histological signs of osteoporosis in OVX mice. Representative images of hematoxylin and eosin staining (top) and TRAP staining (bottom) of mouse femur sections. PS-EM treatment mitigated bone loss compared to PBS as highlighted by black arrows and reduced TRAP expression as indicated by red arrows. Scale bars = 500 μm (top), 100 μm (middle & bottom).

long bone regions, indicating high bone metabolism and activity. When compared to the uptake of ^{18}F-fluoride in the bones of sham mice, the ^{18}F-fluoride in the bones of OVX mice was significantly decreased. However, the treatment with PS-EM and PS-EM-AMG487 effectively mitigated bone loss in the OVX mice, as indicated by the restoration of bone density in Figure 5B.

The μCT images also revealed a substantial bone loss in the vehicle-injected group compared to those of sham mice as illustrated in Figure 5C. Treatment with EMs resulted in a modest restoration of trabecular bone. However, the groups injected with PS-EM or PS-EM-AMG487 demonstrated a notable restoration of trabecular bone, as observed in the 3D reconstruction of mouse femurs (Figure 5C). To quantify the bone parameters, a comprehensive 3D microarchitecture analysis was performed for the mouse femurs. As shown in Figure 5D, bone mineral density (BMD), trabecular bone volume/tissue volume (BV/TV), cortical thickness (Ct.Th.), trabecular thickness (Tb.Th.), trabecular numbers (Tb.N.), and trabecular separation (Tb.Sp.) were analyzed among different groups. EM treatment increased BMD and BV/TV compared to vehicle control (PBS), but there were no significant changes in other parameters. Notably, PS-EMs and PS-EM-AMG487s significantly increased BV/TV, Tb.N., Tb.Th., and decreased Tb.Sp. compared to vehicle control. The trabecular and cortical bone masses were clearly increased in the treatment group, as evidenced by higher Ct. Th. and BMD. Interestingly, similar results were observed when comparing the PS-EM and PS-EM-AMG487 groups to the EM treatment group. The treatment with PS-EM and PS-EM-AMG487 proved to be more effective in inhibiting bone loss compared to EM treatment, as evidenced by increased Tb.Th., Tb.N., and Tb.Sp. The mean value of Tb. N. and Tb. Th. was slightly higher, and the mean value of Tb.Sp. in the PS-EM-AMG487 group was slightly lower than that in the PS-EM group, but there was no significant difference between the two groups.

The results of histological analyses were consistent with the μCT, where H&E staining revealed apparent trabecular bone loss in OVX mice; however, bone loss was significantly restored in

OVX mice treated with PS-EMs and PS-EM-AMG487s as shown in **Figure 6**. TRAP staining indicated that injection of PS-EMs and PS-EM-AMG487s decreased osteoclast number in trabecular bones of osteoporotic mice. Collectively, these data suggest that PS-EM-AMG487 attenuates bone loss in osteoporotic mice. The administration of our particles effectively attenuated bone loss in the OVX mouse model, especially the trabecular bone structures. Interestingly, MSC-derived EMs showed only a hint of attenuating bone loss in OVX mice. PS-incorporated EMs and PS-EMs encapsulating AMG487, on the other hand, exhibited a statistically significant effect in hindering bone loss. AMG487 treatment groups reduced the number of osteoclast precursor cells at the sites of bone resorption (Figure S7, Supporting Information). However, the beneficial effect of AMG487 in PS-EM was not significant in reducing bone loss than expected. It is possible that the progenitor recruitment effect was overwhelmed by the strong inhibitory effect of PS-EMs on osteoclast differentiation and osteoclast activation played more important roles in regulating bone remodeling. In addition, the chemokine receptor CXCR3 is also expressed in lymphocytes. Recent osteoimmunology studies indicate the regulatory roles of T cell cytokines in osteoclastogenesis and pathologic bone remodeling.[54] Future studies will further evaluate the effect of AMG487 and CXCR signaling on these cells in osteoporosis. These data support our hypothesis that the functionalization of EMs using PS and drug loading enhances the effectiveness of EMs in treating osteoporosis. We also performed histopathological examinations to evaluate the biosafety of PS-EMs-AMG487 in healthy mice (Figure S8, Supporting Information). No obvious structural damage or necrosis was found in the major organs (heart, liver, spleen, lung, and kidney) 7 days after administration of PS-EMs or PS-EMs-AMG487. Long-term efficacy and safety studies will be needed for the potential clinical translation of PS-EM-based systems.

Ovariectomy-induced osteoporosis in female rodents is the most commonly used preclinical animal model that exhibits the characteristics of estrogen-deficient human skeleton and postmenopausal osteoporosis. However, some limitations exist

related to the use of OVX animal models.[55–57] The long bones of mature rodents may have open epiphyseal plates and continue to grow, resulting in misinterpretation of skeleton response to OVX. This problem can be addressed by using aged animals (6–9 months old) or skeletal sites with low longitudinal growth (e.g., lumber vertebrae). Another limitation of the OVX model is the use of female animals and the clinical feature of osteoporosis in men is not well appreciated. Future research could be conducted in consideration of such important variables to better reflect the diverse patient population affected by osteoporosis.

3. Conclusion

In this study, we introduced a novel therapeutic strategy employing phosphatidylserine-incorporated exosome mimetics (PS-EMs) to treat osteoporosis. The careful physicochemical characterization of PS-EMs established their consistency and biological relevance, while the preferential uptake by macrophages over MSCs highlighted the targeted action of the PS-EMs. Significantly, the PS-EMs not only inhibited osteoclastogenesis in vitro but also demonstrated a substantial potential to mitigate bone loss in an OVX mouse model, outperforming the pristine EMs. These findings underscore the utility of PS-EMs as functional drug delivery systems, with PS-EM-AMG487 exhibiting pronounced effectiveness in addressing osteoclast-driven conditions.

Surface engineering of PS-EMs to incorporate specific targeting elements holds great promise for future research. The straightforward and adaptable nature of the extrusion technique employed in producing PS-EMs enables easy modifications in the fabrication process. For instance, the use of biorthogonal engineering, particularly copper-free click chemistry, offers an efficient route for precise bioconjugation.[58] Bone-targeting ligand alendronate,[49] cell-specific peptide,[59] or aptamer[60–62] can be effectively attached to the EMs' surface via conjugation. Future studies focusing on these modifications could potentially reduce off-target side effects and enhance the efficacy of PS-EMs.

This study serves as a proof-of-concept for harnessing exosomal nanoparticles to modulate bone resorption through a membrane fusion approach, advancing them as a novel therapeutic option for osteoporosis and related bone diseases. Given that menopausal osteoporosis, rheumatoid arthritis, and periodontitis share common pathologic features such as up-regulated pro-inflammatory cytokines,[63] the application of PS-EMs in these conditions could offer a multifaceted therapeutic opportunity.

4. Experimental Section

Materials: A total of 1,2-dioleoyl-sn-glycero-3-phospho-L-serine (sodium salt) (DOPS), 1,2-dioleoyl-sn-glycero-3-phosphocholine (DOPC), N-(7-Nitrobenz-2-Oxa-1,3-Diazol-4-yl)- 1,2-Dihexadecanoyl-sn- Glycero-3-Phosphoethanolamine (NBD-PE, excitation/emission = 463/536 nm) and Lissamine Rhodamine B 1,2- Dihexadecanoyl-*sn*-Glycero-3-Phosphoethanolamine, Triethylammonium Salt (rhodamine DHPE, excitation/emission = 560/580 nm) were from Avanti Polar Lipids (Alabaster, AL). All of the other chemicals used in the experiments described here were also analytical-grade and used without further purification.

Cell Culture: RAW264.7 cells, a mouse leukemic monocyte/macrophage cell line, and mouse MSCs (D1 ORL UVA, ATCC, VA) were purchased from ATCC (Manassas, VA) and maintained in DMEM supplemented with 10% FBS, penicillin (100 units mL^{-1}) and streptomycin (100 µg mL^{-1}) at 37 °C in a humidified 5% CO$_2$ atmosphere. Bone marrow-derived macrophages were isolated from five-to seven-week-old C57BL/6J mice following the protocol[64] and cultured in DMEM/F-12 medium supplemented with 10% FBS, penicillin (100 units mL^{-1}), streptomycin (100 µg mL^{-1}), and macrophage colony-stimulating factor (25 ng mL^{-1}).

Preparation of MSC-Derived EMs and PS-EMs: Based on a previous report, the MSC-derived EMs were fabricated using a serial extrusive approach.[34] Briefly, the cell suspensions (1 × 10^6 cells mL^{-1}) were passed sequentially through a mini-extruder (Avanti Polar Lipids, Alabaster, AL) using 1- and 5-µm polycarbonate membrane filters (Whatman Inc., Clifton, NJ). PS-EMs were prepared using a thin-film hydration technique. Cell debris and microvesicles of the final extruded sample (1 mL) were removed by centrifugation at 10 000 g for 10 min at room temperature. The exosome mimetics were purified and concentrated with a 100 kDa centrifugal filter (EMD Millipore, Temecula, CA, USA) at 1000 g for 15 min at room temperature with PBS (pH 7.4), repeated three times with an equivalent volume of PBS. The final EM concentration was measured using a Pierce BCA protein assay kit (Thermo Fisher Scientific, Waltham, MA). The ratio of liposome (based on lipid weights) to exosome (based on protein weights) was optimized to 10:1. Lipids were dissolved in chloroform and subsequently evaporated to solvent evaporation under a nitrogen stream. The resulting 1 mg lipid thin film was then hydrated with PBS containing a 0.1 mg protein equivalent of EM, with agitation. The dispersion was further extruded through 0.2-µm polycarbonate membrane filters (Avanti Polar Lipids, Alabaster, AL) to produce lipid-incorporated EM vesicles. The size distribution and concentration of the prepared particles were determined using a NanoSight NS 300 (Malvern Panalytical, Malvern, United Kingdom) with a 532 nm laser. The size, zeta potential, and PDI of the prepared particles were measured on a Zetasizer Nano ZS instrument (Malvern Panalytical, Malvern, United Kingdom).

Cryo-Electron Microscopy: A total of 2.5 mL of LNP solution was applied onto a Quantifoil 200 mesh grid coated with thin carbon film (Ted Pella). Grids were blotted for 2 seconds with filter paper, then were plunged into liquid ethane using a manual plunger. The image was collected on an FEI Tecnai TF20 high-resolution Transmission Electron Microscope at an accelerating voltage of 200 kV. The instrument is equipped with a K2 Direct Detection Camera.

FRET Study: To conduct the Forester resonance energy transfer (FRET) study, two lipophilic dyes were employed: NBD-PE (excitation/emission = 463/536 nm) and rhodamine-DHPE (excitation/emission = 560/580 nm). 1 mol% of both dyes were added during the lipid thin film preparation process; dyes were dissolved in chloroform and subsequently evaporated in a glass vial to form a thin film. For fluorescence measurements, samples were scanned for fluorescence spectra with the PTI QuantaMaster 400 fluorometer (Horiba Scientific, Kyoto, Japan). To acquire an emission spectrum, the sample was excited at 460 nm with an emission scan between 500 and 650 nm. The excitation bandwidth was 10 nm, and the background signal of the PBS buffer was subtracted from the FRET spectrum.

Cytotoxicity: The cytotoxicity of PS-EMs on RAW264.7 cells was assessed using Alamar blue assay. PS-EMs were incubated in a growth medium (DMEM, 10% FBS, 1% P/S) for 24 h. The medium was then replaced with Alamar blue solution (10% v/v) in the growth medium. After a 3-h incubation, the fluorescence intensity of Alamar blue was measured at 570/585 nm (excitation/emission).

Cellular Uptake Assay: hMSCs and RAW264.7 cells were co-cultured in a 1:4 number ratio on NuncLab-Tek II chambered coverglass (Thermo Scientific, Walthan, MA). Rhodamine-labeled EMs were resuspended in an FBS-free DMEM medium and incubated with the cells for 2 or 24 h. Following the incubation, the cells were washed, stained with Hoechst 33 342, and imaged using a Zeiss 710 confocal microscope. Quantitative analysis of cellular uptake was conducted using FIJI Image J software.

TRAP Assay: RAW264.7 cells were seeded at a density of 10^4 cells/well into 24-well plates and incubated for 5 days in an osteoclast differentiation medium supplemented with 100 ng mL^{-1} of RANKL. The medium was further supplemented with EM or control PBS, respectively. On day 5, cells were fixed in 4% paraformaldehyde for 20 min and subsequently stained using a TRAP staining kit (Sigma-Aldrich, St. Louis, MO) following the manufacturer's recommended protocol. Stained cells were imaged using an Olympus IX71 microscope, and osteoclast-like cells, identified by their multinucleation and TRAP-positive status (more than three nuclei), were scored.

Migration Assay: Osteoclast precursors were cultured in α-MEM/10% FBS with 50 ng mL^{-1} M-CSF. After 48 h, cells were harvested and resuspended into serum-free α-MEM. Cells were seeded at 5×10^4 cells into the upper chamber of a 24-well QCM Chemotaxis well plate (ECM506, EMD Millipore Corp, Billerica, MA). The lower well was loaded with α-MEM/10% FBS containing 100 ng mL^{-1} of CXCL9. After 8 h of incubation, the upper membrane surface was washed with PBS, and residual cells were gently removed with a cotton wool swab. Cells that migrated to the bottom side of the membrane were fixed in 4% paraformaldehyde for 20 min and stained with hematoxylin. Quantification of migrated cells was performed with an Olympus IX71 microscope (Olympus Corporation, Tokyo, Japan).

qRT-PCR: The total RNA was extracted from RAW264.7 cells using Trizol reagent (Life Technologies) and an RNeasy mini kit (Qiagen, CA) following the manufacturer's protocol. Subsequently, a 100 ng aliquot of RNA from each sample was reverse transcribed to cDNA using a SuperScript III first-strand synthesis system (Life Technologies). qRT-PCR analysis was subsequently performed with 20 µL of a SYBR Green reaction system in a LightCycler480 PCR instrument (Roche, IN, USA). GAPDH was used as an internal control to normalize signals for each target gene. Gene-specific primer sequences: *CTSK* (F: CTC GGC GTT TAA TTT GGG AGA, R: TCG AGA GGG AGG TAT TCT GAG T), *NFATc1* (F: GCC TTT TGC GAG CAG TAT CTG, R: GCT GCA CCT CGA TCC GAA G), *TRAP* (F: CAC TCC CAC CCT GAG ATT TGT, R: CAT CGT CTG CAC CGT TCT G), *GAPDH* (F: AGG TCG GTG TGA ACG GAT TTG, R: TGT AGA CCA TGT AGT TGA GGT CA).

Luciferase Gene Reporter Assay of NF-κB: RAW264.7 cells were transfected with the NanoLuc reporter vector containing NF-κB (Promega, Madison, WI) and seeded in a 96-well plate at a density of 10^4 cells per well. Cells were pretreated with varying concentrations of PS-EMs for 1 h and then stimulated with 100 ng mL^{-1} of RANKL for 24 h. Subsequently, cells were washed and lysed using 1x lysis buffer. Luciferase activity was quantified using a Nano-Glo Luciferase Assay System according to the manufacturer's instructions (Promega, Madison, WI).

Western Blot Assay: Cells were collected, lysed, and extracted using whole cell lysis buffer (Sigma-Aldrich), supplemented with a 1:100 v/v protease inhibitor cocktail for 1 h on ice. The protein concentration was measured colorimetrically using Bio-Rad reagents. Subsequently, 25 µg of total proteins were resolved and separated on a 12.5% SDS-PAGE gel, followed by transfer onto a polyvinylidene difluoride (PVDF) membrane using a Bio-Rad semidry transfer system. After the transfer, the membrane underwent blocking with 5% dry milk in TBS/Tween20 (TBST) buffer at RT for 1 h and then incubated with primary antibodies diluted in TBST buffer with 5% dry milk overnight at 4 °C. Primary antibodies used in this study are p65, p-p65, and β-actin. The membranes were washed with TBST buffer and exposed to secondary antibodies for 1 h at RT. After washing, membrane signals were detected using Pierce ECL reagents and Bio-Rad ChemiDoc MP system.

Ovariectomized Mouse Model: Eight-week-old Female C57BL/6J mice were obtained from the Jackson Laboratories (Bar Harbor, ME). Eighteen mice underwent bilateral ovariectomy, while three mice underwent a sham operation. Two weeks post-OVX, the mice were randomly divided into four groups (PBS control, EM, PS-EM, PS-EM-AMG487). Each group received 100 µL of EM, PS-EM, PS-EM-AMG-487 (1 mg mL^{-1}) or an equal volume of PBS, respectively, administered intraperitoneally once a week for 8 weeks. All experiments on mice were performed under a protocol approved by the Animal Research Committee and in accordance with UCLA's institutional policy on the humane and ethical treatment of animals.

PET/CT Study: Live computed tomography/positron emission tomography (CT/PET) studies were performed as follows. Animals were anesthetized with 1.5% vaporized isoflurane, and injected with 18F-FDG via tail vein. After 60 min 18F-FDG uptake under conscious conditions, animals underwent microPET imaging (10 min static data acquisition) immediately followed by microCT imaging using the Genisys8 PET/CT scanner (Sofie Biosciences, Culver City, CA). PET data were decay corrected, and attenuation correction was performed using the CT images. Co-registered PET/CT data were analyzed using AMIDE software.

MicroCT Scanning and Analysis: At 1 week after injection, mice were sacrificed, and the femurs of each group were collected for further analysis. The specimens were fixed in 4% paraformaldehyde for two days and subsequently scanned at 80 kVp/140 µA with 500 ms exposure and a 5-frame average at a resolution of 20 µm using a µCT scanner (HiCT) developed by the Chatziioannou Lab at the Crump Institute for Molecular Imaging at UCLA. 3D reconstruction and analysis of the µCT images were performed using the Dragonfly software (Version 2022. 2 for Windows; Comet Technologies Canada Inc., Montréal, Canada) with DICOM files. The volume of interest of trabecular bone was taken 0.5 mm proximally from the distal epiphyseal growth plate, with 3 mm in height. The following parameters were collected: BV/TV (%), Tb.Th., Tb.N., Tb.Sp., Ct.Th., and BMD.

Bone Histomorphometric Analysis: After microCT scanning, fixed tissues underwent a 7-day incubation in 10% EDTA solution with gentle shaking, refreshed once on day 3. Following decalcification, samples were embedded in paraffin and sectioned into 5 µm-thick slices. Histological assessments were performed using H&E staining for general morphology and TRAP staining to identify osteoclasts using an Olympus IX71 microscope (Olympus Corporation, Tokyo, Japan).

Statistical Analysis: Data were presented as mean ± SD for all results. Statistical significance was determined by a two-tailed *t*-test or one-way analysis of variance (ANOVA) with Tukey using GraphPad Prism 10 software (GraphPad, San Diego, CA, USA). $^*p < 0.05$, $^{**}p < 0.01$, and $^{***}p < 0.001$ were considered statistically significant.

Supporting Information

Supporting Information is available from the Wiley Online Library or from the author.

Acknowledgements

Conflict of Interest

The authors declare no conflict of interest.

Author Contributions

The manuscript was written through the contributions of all authors. All authors approved the final version of the manuscript.

Data Availability Statement

The data that support the findings of this study are available from the corresponding author upon reasonable request.

Keywords

[1] Consensus development conference: Diagnosis, prophylaxis, and treatment of osteoporosis, *Am. J. Med.* **1993**, *94*, 646.

[2] N. Harvey, E. Dennison, C. Cooper, *Nat. Rev. Rheumatol.* **2010**, *6*, 99.

[3] M. K. Skjødt, M. Frost, B. Abrahamsen, *Brit. J. Clinical Pharma.* **2019**, *85*, 1063.

[4] A. A. Khan, A. Morrison, D. L. Kendler, R. Rizzoli, D. A. Hanley, D. Felsenberg, L. K. McCauley, F. O'Ryan, I. R. Reid, S. L. Ruggiero, A. Taguchi, S. Tetradis, N. B. Watts, M. L. Brandi, E. Peters, T. Guise, R. Eastell, A. M. Cheung, S. N. Morin, B. Masri, C. Cooper, S. L. Morgan, B. Obermayer-Pietsch, B. L. Langdahl, R. A. Dabagh, K. S. Davison, G. K. Sándor, R. G. Josse, M. Bhandari, M. El Rabbany, et al., *J. Clin. Densit.* **2017**, *20*, 8.

[5] W. Zhang, L. Gao, W. Ren, S. Li, J. Zheng, S. Li, C. Jiang, S. Yang, K. Zhi, *Front. Immunol.* **2021**, *12*, 606043.

[6] C.-H. Lu, Y.-A. Chen, C.-C. Ke, R.-S. Liu, *IJMS* **2021**, *22*, 12750.

[7] J. Kowal, M. Tkach, C. Théry, *Curr. Opin. Cell Biol.* **2014**, *29*, 116.

[8] S. El Andaloussi, S. Lakhal, I. Mäger, M. J. A. Wood, *Adv. Drug Delivery Rev.* **2013**, *65*, 391.

[9] L. Kordelas, V. Rebmann, A.-K. Ludwig, S. Radtke, J. Ruesing, T. R. Doeppner, M. Epple, P. A. Horn, D. W. Beelen, B. Giebel, *Leukemia* **2014**, *28*, 970.

[10] P. Zhao, L. Xiao, J. Peng, Y.-Q. Qian, C.-C. Huang, *Euro. Rev. Med. Pharmacol. Sci.* **2018**, *22*, 3962.

[11] R. Zuo, M. Liu, Y. Wang, J. Li, W. Wang, J. Wu, C. Sun, B. Li, Z. Wang, W. Lan, C. Zhang, C. Shi, Y. Zhou, *Stem Cell Res. Ther.* **2019**, *10*, 30.

[12] G. Lu, P. Cheng, T. Liu, Z. Wang, *Front. Cell Dev. Biol.* **2020**, *8*, 608521.

[13] F. Xiao, B. Zuo, B. Tao, C. Wang, Y. Li, J. Peng, C. Shen, Y. Cui, J. Zhu, X. Chen, *Ann. Transl. Med.* **2021**, *9*, 798.

[14] E. J. Bunggulawa, W. Wang, T. Yin, N. Wang, C. Durkan, Y. Wang, G. Wang, *J. Nanobiotechnol.* **2018**, *16*, 81.

[15] D. Jafari, S. Shajari, R. Jafari, N. Mardi, H. Gomari, F. Ganji, M. Forouzandeh Moghadam, A. Samadikuchaksaraei, *BioDrugs* **2020**, *34*, 567.

[16] M. Kang, C.-S. Lee, M. Lee, *Bioengineering* **2021**, *8*, 137.

[17] J. Rezaie, M. Feghhi, T. Etemadi, *Cell Commun. Signal* **2022**, *20*, 145.

[18] Y. T. Sato, K. Umezaki, S. Sawada, S. Mukai, Y. Sasaki, N. Harada, H. Shiku, K. Akiyoshi, *Sci. Rep.* **2016**, *6*, 21933.

[19] M. Piffoux, A. K. A. Silva, C. Wilhelm, F. Gazeau, D. Tareste, *ACS Nano* **2018**, *12*, 6830.

[20] Y. Lin, J. Wu, W. Gu, Y. Huang, Z. Tong, L. Huang, J. Tan, *Adv. Sci.* **2018**, *5*, 1700611.

[21] J. G. Kay, M. Koivusalo, X. Ma, T. Wohland, S. Grinstein, *MBoC* **2012**, *23*, 2198.

[22] R. B. Birge, S. Boeltz, S. Kumar, J. Carlson, J. Wanderley, D. Calianese, M. Barcinski, R. A. Brekken, X. Huang, J. T. Hutchins, B. Freimark, C. Empig, J. Mercer, A. J. Schroit, G. Schett, M. Herrmann, *Cell Death Differ.* **2016**, *23*, 962.

[23] U. Harre, H. Keppeler, N. Ipseiz, A. Derer, K. Poller, M. Aigner, G. Schett, M. Herrmann, K. Lauber, *Autoimmunity* **2012**, *45*, 612.

[24] J.-H. Kang, H.-M. Ko, G.-D. Han, S.-Y. Lee, J.-S. Moon, M.-S. Kim, J.-T. Koh, S.-H. Kim, *Cell Death Dis.* **2020**, *11*, 497.

[25] R. Toita, J.-H. Kang, A. Tsuchiya, *Acta Biomater.* **2022**, S174270612200681X.

[26] Z. Wu, H. M. Ma, T. Kukita, Y. Nakanishi, H. Nakanishi, *J.I* **2010**, *184*, 3191.

[27] S. Rodriguez-Fernandez, I. Pujol-Autonell, F. Brianso, D. Perna-Barrull, M. Cano-Sarabia, S. Garcia-Jimeno, A. Villalba, A. Sanchez, E. Aguilera, F. Vazquez, J. Verdaguer, D. Maspoch, M. Vives-Pi, *Front. Immunol.* **2018**, *9*, 253.

[28] M. E. Klein, S. Mauch, M. Rieckmann, D. G. Martínez, G. Hause, M. Noutsias, U. Hofmann, H. Lucas, A. Meister, G. Ramos, H. Loppnow, K. Mäder, *NBM* **2020**, *23*, 102096.

[29] Q. T. Phan, W. H. Tan, R. Liu, S. Sundaram, A. Buettner, S. Kneitz, B. Cheong, H. Vyas, S. Mathavan, C. Schartl, C. Winkler, *Proc. Natl. Acad. Sci.* **2020**, *117*, 19276.

[30] S. A. Bakheet, M. A. Ansari, A. Nadeem, S. M. Attia, A. R. Alhoshani, G. Gul, Q. H. Al-Qahtani, N. A. Albekairi, K. E. Ibrahim, S. F. Ahmad, *Cellular Signalling* **2019**, *64*, 109395.

[31] Z. Liu, W. Liang, D. Kang, Q. Chen, Z. Ouyang, H. Yan, B. Huang, D. Jin, Y. Chen, Q. Li, *CIA* **2020**, *15*, 1201.

[32] T. Hasegawa, V. Venkata Suresh, Y. Yahata, M. Nakano, S. Suzuki, S. Suzuki, S. Yamada, H. Kitaura, I. Mizoguchi, Y. Noiri, K. Handa, M. Saito, *Sci. Rep.* **2021**, *11*, 2613.

[33] M. Wijtmans, D. Verzijl, R. Leurs, I. J. P. de Esch, M. J. Smit, *ChemMedChem* **2008**, *3*, 861.

[34] J. Fan, C.-S. Lee, S. Kim, C. Chen, T. Aghaloo, M. Lee, *ACS Nano* **2020**, *14*, 11973.

[35] S. C. Jang, O. Y. Kim, C. M. Yoon, D.-S. Choi, T.-Y. Roh, J. Park, J. Nilsson, J. Lötvall, Y.-K. Kim, Y. S. Gho, *ACS Nano* **2013**, *7*, 7698.

[36] W. Jo, J. Kim, J. Yoon, D. Jeong, S. Cho, H. Jeong, Y. J. Yoon, S. C. Kim, Y. S. Gho, J. Park, *Nanoscale* **2014**, *6*, 12056.

[37] X. Han, S. Shen, Q. Fan, G. Chen, E. Archibong, G. Dotti, Z. Liu, Z. Gu, C. Wang, *Sci. Adv.* **2019**, *5*, eaaw6870.

[38] A. Kim, W. B. Ng, W. Bernt, N.-J. Cho, *Sci. Rep.* **2019**, *9*, 2639.

[39] M. Danaei, M. Dehghankhold, S. Ataei, F. Hasanzadeh Davarani, R. Javanmard, A. Dokhani, S. Khorasani, M. Mozafari, *Pharmaceutics* **2018**, *10*, 57.

[40] R. B. Sekar, A. Periasamy, *J. Cell Biol.* **2003**, *160*, 629.

[41] N. K. Shah, S. K. Gupta, Z. Wang, S. A. Meenach, *J. Drug Deliv. Sci. Technol.* **2019**, *50*, 57.

[42] C. Lo Sicco, D. Reverberi, C. Balbi, V. Ulivi, E. Principi, L. Pascucci, P. Becherini, M. C. Bosco, L. Varesio, C. Franzin, M. Pozzobon, R. Cancedda, R. Tasso, *Stem Cells Transl. Med.* **2017**, *6*, 1018.

[43] M. Ashrafuzzaman, H. A. M. AlMansour, M. A. S. AlOtaibi, Z. Khan, G. M. Shaik, *Membranes* **2021**, *12*, 37.

[44] K. Doffek, X. Chen, S. L. Sugg, J. Shilyansky, *Mol. Immunol.* **2011**, *48*, 1771.

[45] K. S. Lee, J. Lee, H. K. Kim, S. H. Yeom, C. H. Woo, Y. J. Jung, Y. E. Yun, S. Y. Park, J. Han, E. Kim, J. H. Sul, J. M. Jung, J. H. Park, J. S. Choi, Y. W. Cho, D. Jo, *J. Extracell. Vesicles* **2021**, *10*.

[46] L. Wu, Y. Kim, G. M. Seon, S. H. Choi, H. C. Park, G. Son, S. M. Kim, B.-S. Lim, H.-C. Yang, *Biomaterials* **2021**, *279*, 121239.

[47] Q. Ge, Y. Zhou, J. Lu, Y. Bai, X. Xie, Z. Lu, *Molecules* **2014**, *19*, 1568.

[48] A. Jeyaram, S. M. Jay, *AAPS J.* **2018**, *20*, 1.

[49] C.-S. Lee, J. Fan, H. S. Hwang, S. Kim, C. Chen, M. Kang, T. Aghaloo, A. W. James, M. Lee, *Nano Lett.* **2023**, *23*, 1202.

[50] Y. Hu, R. Xu, C.-Y. Chen, S.-S. Rao, K. Xia, J. Huang, H. Yin, Z.-X. Wang, J. Cao, Z.-Z. Liu, Y.-J. Tan, J. Luo, H. Xie, *Metabolism* **2019**, *95*, 93.

[51] H. Song, X. Li, Z. Zhao, J. Qian, Y. Wang, J. Cui, W. Weng, L. Cao, X. Chen, Y. Hu, J. Su, *Nano Lett.* **2019**, *19*, 3040.

[52] C. Sheng, X. Guo, Z. Wan, X. Bai, H. Liu, X. Zhang, P. Zhang, Y. Liu, W. Li, Y. Zhou, L. Lv, *Nano Res.* **2022**, *15*, 9135.

[53] P. Liu, G. Chen, J. Zhang, *Molecules* **2022**, *27*, 1372.

[54] W. Zhang, K. Dang, Y. Huai, A. Qian, *Front. Endocrinol.* **2020**, *11*, 465.

[55] W. S. Jee, W. Yao, *J Musculoskelet Neuronal Interact* **2001**, *1*, 193.

[56] N. Yousefzadeh, K. Kashfi, S. Jeddi, A. Ghasemi, *EXCLI J* **2020**, *19*, 89.

[57] Department of Clinical Sciences, Colorado State University, Ft. Collins, CO 80523, USA, A. Simon Turner, *eCM* **2001**, *1*, 66.

[58] J. P. K. Armstrong, M. N. Holme, M. M. Stevens, *ACS Nano* **2017**, *11*, 69.

**ADVANCED
SCIENCE NEWS**

www.advancedsciencenews.com

**ADVANCED
FUNCTIONAL
MATERIALS**

www.afm-journal.de

[59] Q. Meng, Z. Man, L. Dai, H. Huang, X. Zhang, X. Hu, Z. Shao, J. Zhu, J. Zhang, X. Fu, X. Duan, Y. Ao, *Sci. Rep.* **2015**, *5*, 17802.

[60] C. Liang, B. Guo, H. Wu, N. Shao, D. Li, J. Liu, L. Dang, C. Wang, H. Li, S. Li, W. K. Lau, Y. Cao, Z. Yang, C. Lu, X. He, D. W. T. Au, X. Pan, B.-T. Zhang, C. Lu, H. Zhang, K. Yue, A. Qian, P. Shang, J. Xu, L. Xiao, Z. Bian, W. Tan, Z. Liang, F. He, L. Zhang, et al., *Nat. Med.* **2015**, *21*, 288.

[61] Z.-W. Luo, F.-X.-Z. Li, Y.-W. Liu, S.-S. Rao, H. Yin, J. Huang, C.-Y. Chen, Y. Hu, Y. Zhang, Y.-J. Tan, L.-Q. Yuan, T.-H. Chen, H.-M. Liu, J. Cao, Z.-Z. Liu, Z.-X. Wang, H. Xie, *Nanoscale* **2019**, *11*, 20884.

[62] M. Wang, H. Wu, Q. Li, Y. Yang, F. Che, G. Wang, L. Zhang, *IJN* **2019**, *14*, 8707.

[63] C. O. Bingham, M. Moni, *Curr. Opin. Rheumatol.* **2013**, *25*, 345.

[64] X. Zhang, R. Goncalves, D. M. Mosser, *CP in Immunology* **2008**, *83*.